

# INVESTIGATION AND APPLICATION OF INVERSE DETERMINATION OF INTERFACIAL HEAT TRANSFER COEFFICIENT IN VACUUM INVESTMENT CASTING

Xu Liu and Ye Wang 

School of Materials Science and Chemical Engineering, Harbin University of Science and Technology, Harbin 150001, China

Hang Zheng and Zhao Guo

Aecc South Industry Company Limited, Zhuzhou 412002, China

Guohuai Liu and Zhaodong Wang

State Key Laboratory of Rolling and Automation, Northeastern University, Shenyang 110819, China

Copyright © 2024 American Foundry Society  
<https://doi.org/10.1007/s40962-023-01240-1>

## Abstract

The interface heat transfer coefficient (IHTC) at the different casting/shell mold interfaces during the vacuum investment casting process was investigated by measuring the temperatures of K4169 superalloy melt and mold shell during the preheating, transferring, pouring, and solidification processes. The inverse model of ProCAST was used to calculate the interface heat transfer coefficient (IHTC) based on the temperature measurement results. The inverse calculation results show that the heat transfer between the shell mold and the outside air changes from natural convection to forced convection during the transfer process, but the heat transfer between the shell mold and the inside air is consistently natural convection heat transfer. Then, the convective heat transfer coefficient gradually decreases to  $0.1 \text{ W/m}^2\cdot\text{K}$  with the vacuum increases and is finally converted to radiation heat transfer at a vacuum of  $10^{-3}$

Pa. In the early stages of solidification, the IHTC between the shell mold and the casting can reach  $16,000 \text{ W/m}^2\cdot\text{K}$  due to the close contact and the large temperature difference between them, and with the thermal expansion of the shell mold and cooling contraction of the casting, the formation of the gap leads to the interfacial heat transfer coefficient gradually stabilizing at  $100\text{--}200 \text{ W/m}^2\cdot\text{K}$ . The experimental validation results show that the IHTC has a great influence on the accuracy of the prediction of the location and shape of shrinkage porosities in the vacuum investment castings.

**Keywords:** vacuum investment casting, temperature measurement, nickel-based superalloy, interface heat transfer coefficient, inverse calculation

## Introduction

Nickel-based superalloys are widely used for components in aerospace engines such as blades, turbine disks, and combustion chambers in high-temperature environments because of their excellent oxidation resistance, strength, creep strength, endurance strength, and good fatigue resistance at high temperature.<sup>1–4</sup> The demand for higher service temperature, large structure-activity ratio, and higher maneuverability of aerospace equipment has

prompted the development of nickel-based superalloy castings in the direction of larger, more complex, and thinner walls.<sup>5–7</sup> Investment casting has been widely used in intricate, thinner walls, and near-net shape with smooth surface.<sup>8</sup> However, casting defects, such as shrinkage porosity, macro-segregation, and hot cracking occurring during the precision casting process of nickel-based superalloys, have seriously affected the service performance of the castings. The optimization of the investment casting process by traditional trial and error methods is often time-consuming and costly, combining numerical simulation with optimization of the investment casting process can save 30–60% in time and 13–30% in cost of

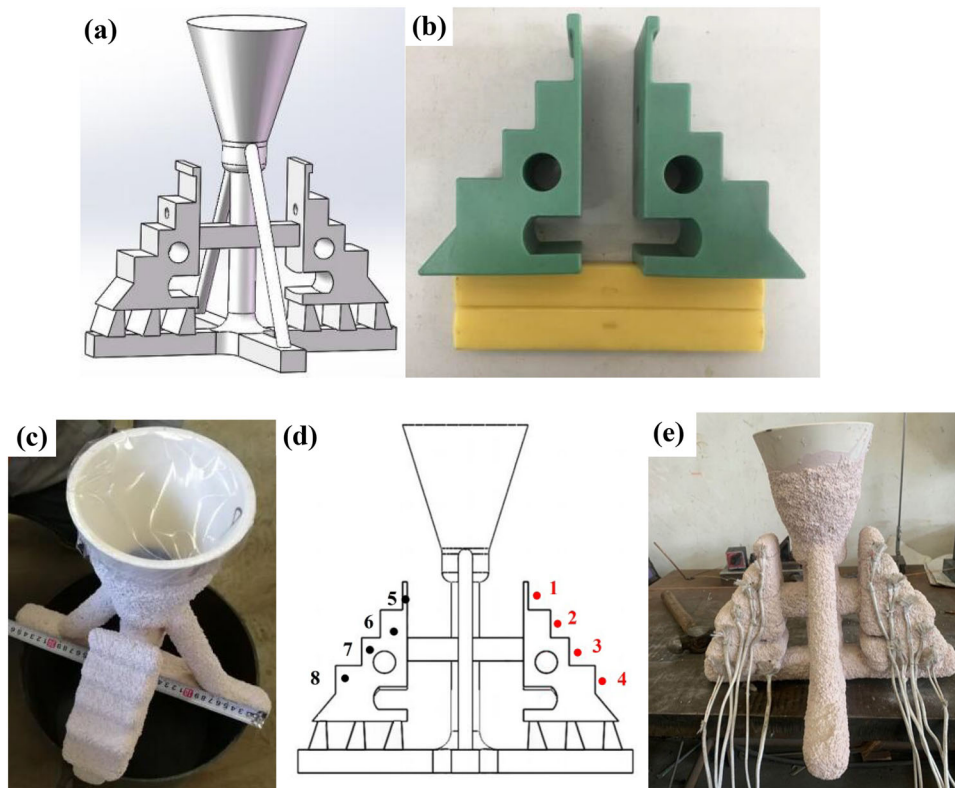


**Figure 1. (a) Schematic diagram of mold, (b) the wax assembly, (c) the ceramic shell mold, (d) the temperature measurement points, and (e) the ceramic shell mold with the thermocouples.**

product development.<sup>9</sup> Therefore, in recent years, many researchers have focused on optimizing the process parameters of vacuum investment casting by simulating the filling and solidification processes of nickel-based alloy castings, so as to effectively predict casting defects and improve casting quality.<sup>10–16</sup>

Obviously, the boundary conditions used for the calculation, including the thermophysical properties of the material and the IHTC between the different materials, are very important for the accurate prediction of the casting process.<sup>17,18</sup> However, compared to the thermophysical parameters of the materials, which can be obtained by measurement, the determination of the IHTC is extremely difficult due to many factors such as solidification conditions, casting structures, gap formation, and so on.<sup>19</sup> Therefore, the IHTC is usually calculated by the inverse method numerically, which is based on the measured temperature, and by constantly adjusting the IHTC (or interface heat flux density) to obtain the simulated temperature closest to the measured temperature, and finally to get the IHTC approaching the actual variation. Szeliga,<sup>20</sup> Shao<sup>21</sup> and Ahmadein et al<sup>22</sup> determined the casting-mold interface heat transfer coefficient of IN 713C superalloy, TC4 alloy, and A356 aluminum alloy by inverse method, respectively, and the validation results of the calculated temperature distributions both matched well with the measured values. However, due to the difficulty of

accurately measuring temperature in a vacuum environment, the heat transfer coefficient at different mold/casting interfaces in the vacuum investment casting process has been rarely studied.

In this study, the temperatures of K4169 superalloy casting and shell mold at different locations during the vacuum investment casting process were obtained by the measurements, and the IHTC of casting-shell mold was obtained by the inverse method combined with temperature measurement results. The results of verification with actual defects showed that the obtained IHTC can accurately predict the defects in vacuum investment casting.

## Methodology

### Experimental Procedure

The temperature measurement device consisted of B-type thermocouples for measuring the metal, N-type thermocouples for measuring the shell mold, and the temperature collector. The 3D model, and wax pattern of the K4169 nickel-based superalloy casting with gating system, and the ceramic shell mold are shown in Figure 1(a) to (c). The wax pattern was first given a (Zircon powder, aluminum cobalt oxide, silica sol and zircon sand) slurry prime coat and the shell mold was made up of ten subsequent layers of

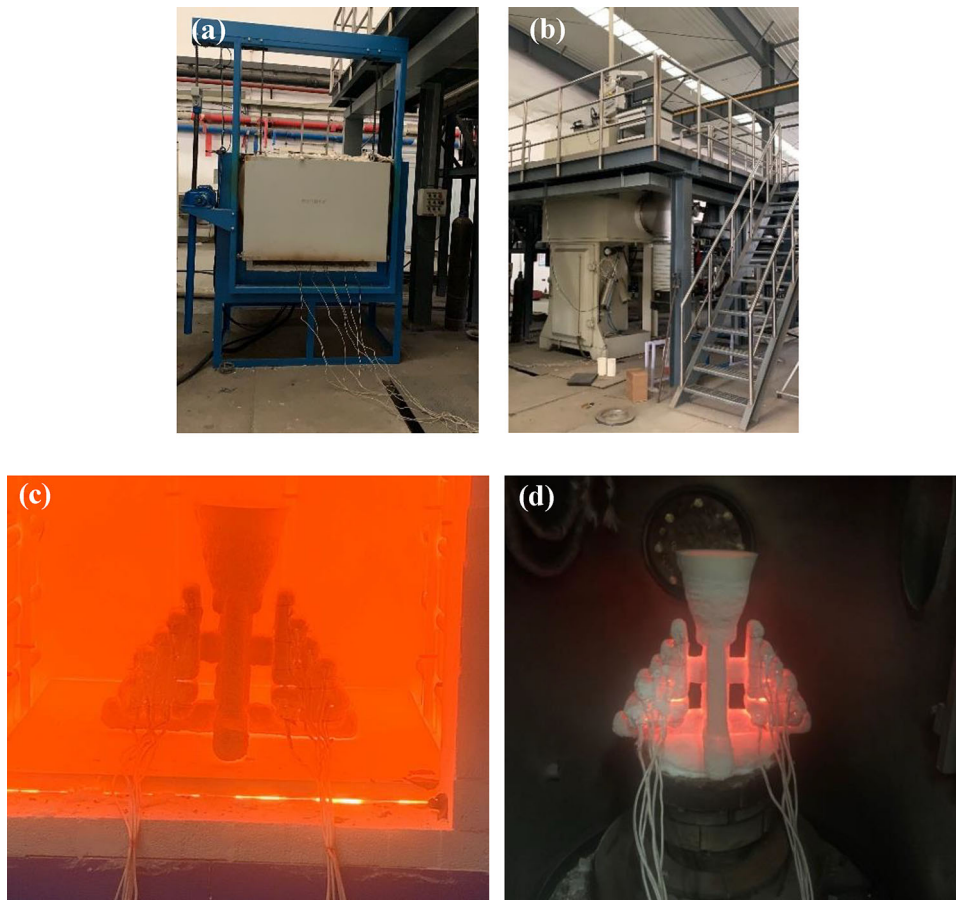


**Figure 2. (a) Preheating furnace and (b) vacuum melting furnaces, (c) preheating process of shell mold, and (d) shell mold for pouring after transfer.**

mullite and corundum sand with an average thickness of 10 mm. The molds were dried, and the wax was continuously melted and removed in an autoclave at proper temperature and pressure. The molds were then preheated to 1050 °C before pouring. During the vacuum investment casting process, the temperature distribution of the shell mold and casting was measured on two identical castings to avoid the interaction of the thermocouples on the shell mold and casting at the same interface, as shown in Figure 1(d) and (e), where the thermocouples 1–4 for measuring the temperature of the shell mold and thermocouples 5–8 for measuring the temperature of the metal. The thermocouples were inserted into the shell mold and the cavity at a depth of 5 mm and 20 mm, respectively.

The K4169 superalloy was melted and refined by vacuum induction melting and poured into the shell mold at 1450 °C in the three-chamber vacuum furnace (DongBo Thermal Technology Co.), as shown in Figure 2(a). The shell mold was preheated to 1050 °C in the GLW-1200LBS box-type furnace as shown in Figure 2(b) and (c), and was subsequently transferred to a vacuum casting chamber, as shown in Figure 2(d). The transfer and vacuum extraction time was about 120 s and the pouring process lasted about 6 seconds. The pouring process was carried out in a vacuum

environment of about  $10^{-3}$  Pa, and then the cooling and solidification process were implemented in the air. All thermocouples were connected to the temperature collector to monitor the temperature variation throughout the whole process of preheated, transfer, vacuum extraction, pouring, and solidification.

### Modeling and Physical Parameters

A 3D finite element (FE) model for inverse calculation was established based on the casting model illustrated in Figure 1(a). The non-homogenized finite element mesh was generated by ProCAST software to ensure the accuracy and efficiency of the simulation.<sup>23,24</sup> The area of casting was divided by a fine mesh from 1 mm to 5 mm the gating system, that the small mesh size can improved accuracy of calculations,<sup>25</sup> and the shell mold were divided by a coarse finite element mesh from 5 mm to 20 mm as shown in Figure 3(a) and (b). The corresponding locations of the temperature measurement points are shown in Figure 3(c). To guarantee the accuracy of the inverse calculation results of the IHTC, the thermophysical properties of all the materials, including thermal conductivity, specific heat, thermal expansion coefficient, density, and emissivity,

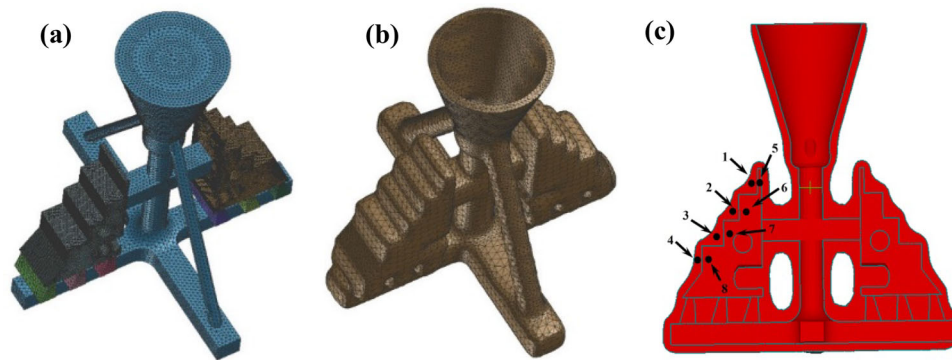


**Figure 3.** The finite element mesh of (a) casting and (b) ceramic shell mold, and (c) corresponding locations of the temperature measurement points.

**Table 1. Temperature-Dependent Thermophysical Properties of K4169 Superalloy**

T (°C)	Coefficient of thermal expansion ( $10^{-6}/^{\circ}\text{C}$ )	Thermal conductivity ( $\text{W}/\text{m}^2\cdot\text{K}$ )	T (°C)	Specific heat ( $\text{kJ}/\text{kg}\cdot\text{K}$ )	Emissivity
800	16.23	26.13	800	0.71	0.70
840	16.73	25.67	850	0.69	0.76
880	17.17	25.37	900	0.68	0.81
920	17.53	27.17	950	0.71	0.83
960	17.63	27.00	1000	0.71	0.86
1000	17.33	28.60	1050	0.74	0.92
1040	16.93	30.07	1100	0.77	–
1080	16.50	34.50	1150	0.86	–
1120	16.20	38.80	1200	0.97	–
1160	15.90	40.90	1250	1.00	–
1200	16.23	42.23	–	–	–

**Table 2. Temperature-Dependent Thermophysical Properties of Ceramic Shell**

T (°C)	Thermal conductivity ( $\text{W}/\text{m}^2\cdot\text{K}$ )	T (°C)	Specific heat ( $\text{kJ}/\text{kg}\cdot\text{K}$ )
800	0.73	800	1.20
900	0.79	850	1.21
1000	0.86	900	1.20
1100	0.95	950	1.21
1200	1.05	1000	1.24
–	–	1050	1.25
–	–	1100	1.31
–	–	1150	1.30
1-	–	1200	1.28
–	–	1250	1.26
–	–	–	–

**Table 3. The Temperature-Dependent Density of K 4169 and Shell**

K 4169		Shell	
Temperature (°C)	Density ( $\text{g}/\text{cm}^3$ )	Temperature (°C)	Density ( $\text{g}/\text{cm}^3$ )
800	7.801	500	2.415
840	7.773	550	2.409
880	7.745	600	2.401
920	7.719	650	2.395
960	7.698	700	2.388
1000	7.688	750	2.382
1040	7.680	800	2.376
1080	7.675	850	2.371
1120	7.667	900	2.366
1160	7.659	950	2.363
1200	7.632	–	–

were measured between 800°C and 1250 °C. The results are listed in Tables 1, 2, 3 and were employed in the inverse calculation. The thermal conductivity, specific heat, and thermal expansion coefficients of the materials were measured by a Netzsch LFA-427 laser flash apparatus, a NETZSCH STA-449 F1 thermal analysis system, and a NETZSCH DIL 402 Expedit Supreme HT, respectively. The emissivity was measured using an AMETEK-Land SPOT-5 combined with contact thermocouples in the vacuum furnace. The density was measured by AU-200ME. Due to the materials, properties above solid temperature were very difficult to measured, The properties above the solid temperature region of 1300 °C to 1500 °C was obtained by the thermodynamic databases in ProCAST as well as in other relevant studies,<sup>10,26,27</sup> the compare of properties of K4169 alloy by calculation and measurement as shows as Figure 4.

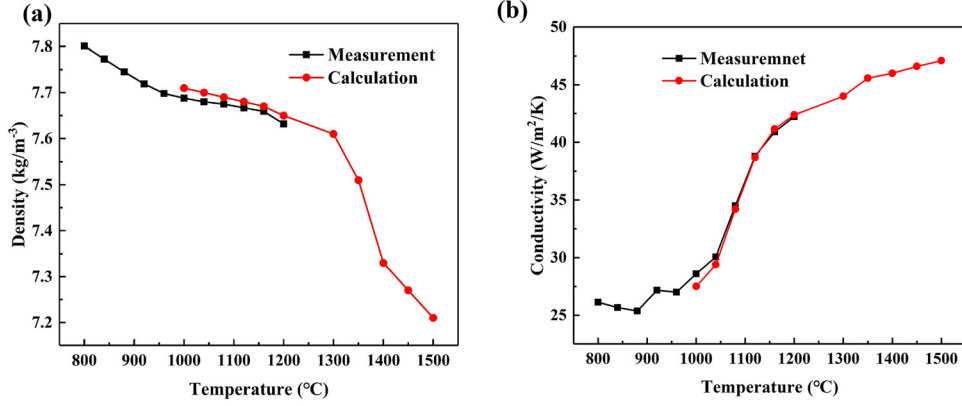


**Figure 4.. The calculation and measurement properties of K 4169 alloy: (a) Density; (b) Conductivity.**

### Inverse Model

In the inverse method, the IHTC can be obtained by solving Eqn. 1<sup>20,28</sup> as follows:

$$h = \frac{q}{T_{\text{casting}} - T_{\text{shell}}} \quad \text{Eqn. 1}$$

where  $h$  is IHTC ( $\text{W}/\text{m}^2 \cdot \text{K}$ ),  $q$  is the heat flux at the casting-shell interface ( $\text{W}/\text{m}^2$ ),  $T_{\text{casting}}$  and  $T_{\text{shell}}$  are the measured temperature ( $^{\circ}\text{C}$ ) of the casting and the shell mold on both sides of the interface.

During the solidification process, influenced by the crystallization latent heat, the heat transfer can be regarded as a non-stationary heat transfer process with a heat source, as described by Eqn. 2:<sup>29</sup>

$$\rho c \frac{\partial T}{\partial t} = \frac{\partial}{\partial x} \left( \lambda \frac{\partial T}{\partial x} \right) + \frac{\partial}{\partial y} \left( \lambda \frac{\partial T}{\partial y} \right) + \frac{\partial}{\partial z} \left( \lambda \frac{\partial T}{\partial z} \right) + q_v \quad \text{Eqn. 2}$$

where the  $\rho$  is density ( $\text{kg}/\text{m}^3$ ),  $c$  is specific heat ( $\text{kJ}/\text{kg}/\text{K}$ ),  $t$  is time (s),  $\lambda$  is thermal conductivity ( $\text{W}/\text{m}^2 \cdot \text{K}$ ),  $q_v$  is the crystallization latent heat released per unit volume of K4169 superalloy per unit time ( $\text{W}/\text{m}^3$ ).

In the inverse calculations process, the criterion for convergence is generally based on the MPA (Maximum A Posteriori) technique<sup>29,30</sup>:

$$S(h) = \sum_{i=1}^{N_t} \sum_{j=0}^{N_s} \frac{1}{\phi_T^2} [T_{ij}^m - T_{ij}^c(h)]^2 + \sum_{k=1}^{N_k} \frac{1}{\phi_k^2} [h_k - h_k^0]^2 \quad \text{Eqn. 3}$$

where  $h$  is IHTC which needs solving by inverse calculation,  $h = h_1, h_2, h_3, \dots, h_k$ .  $N_k$  is the relationship between IHTC and time.  $T_{ij}^m$  is the temperature at measurement points in different time  $t_i$  ( $i = 1, 2, \dots, N_t$ ).  $T_{ij}^c(h)$  is calculation temperature.  $\phi_T$  is the error of measured temperature.  $\phi_k$  is the maximum change value of  $h$  in the iteration process.  $h_k^0$  is assumed initial IHTC.

The  $S(h) = 0$  in the IHTC solve process, so Eqn. 3 can be written as:

$$\frac{\partial S}{\partial h_l} = \sum_{i=1}^{N_t} \sum_{j=0}^{N_s} \frac{-2}{\sigma_T^2} [T_{ij}^m - T_{ij}^c(h)] \cdot X_{ijl} + \frac{2}{\sigma_l^2} [h_l - h_l^0] \quad \text{Eqn. 4}$$

where the  $X_{ijl}$  is sensitivity coefficient, which can be expressed as:

$$X_{ijl} = \frac{\partial T_{ij}^c(h)}{\partial h_l} \approx \frac{T_{ij}^c(h_1, \dots, h_l + \delta h_l, \dots, h_{N_h}) - T_{ij}^c(h_1, \dots, h_l, \dots, h_{N_h})}{\delta h_l} \quad \text{Eqn. 5}$$

where the  $\delta h_l$  is the amount of change in the  $h_l$  of the previous iteration. The temperature of the next iteration  $T_{ij}^c(h^{v+1})$  in the temperature calculation process is also linearized, which can be expressed as:

$$T_{ij}^c(h^{v+1}) \cong T_{ij}^c(h^v) + \sum_{k=1}^{N_h} X_{ijk}^v \cdot \Delta h_k \quad \text{Eqn. 6}$$

The  $\Delta h_k$  is an increment of IHTC:

$$[A] \cdot \Delta h = f \dots \text{or} \dots \sum_{i=1}^{N_t} A_{ik} \cdot \Delta h_k = f_i \quad \text{Eqn. 7}$$

$$A_{ik} = \sum_{i=1}^{N_t} \sum_{j=1}^{N_m} \frac{X_{ijk} \cdot X_{ijl}}{\sigma_T^2} + \frac{\delta_{lk}}{\sigma_l^2} \quad \text{Eqn. 8}$$

$$f_i = \sum_{i=1}^{N_t} \sum_{j=1}^{N_m} \frac{1}{\sigma_T^2} \cdot [T_{ij}^m - T_{ij}^c(h^v)] \cdot X_{ijl} + \frac{1}{\sigma_l^2} [h_l^v - h_l^0] \quad \text{Eqn. 9}$$

where  $\delta_{lk}$  is the Klonk symbol.

According to the Eqns. 6–8, the  $\Delta h_k$  can be calculated directly. Then, the IHTC  $h_k$  in this moment can be calculated by the equation:

$$h_k = h_k^* + \Delta h_k \quad \text{Eqn. 10}$$

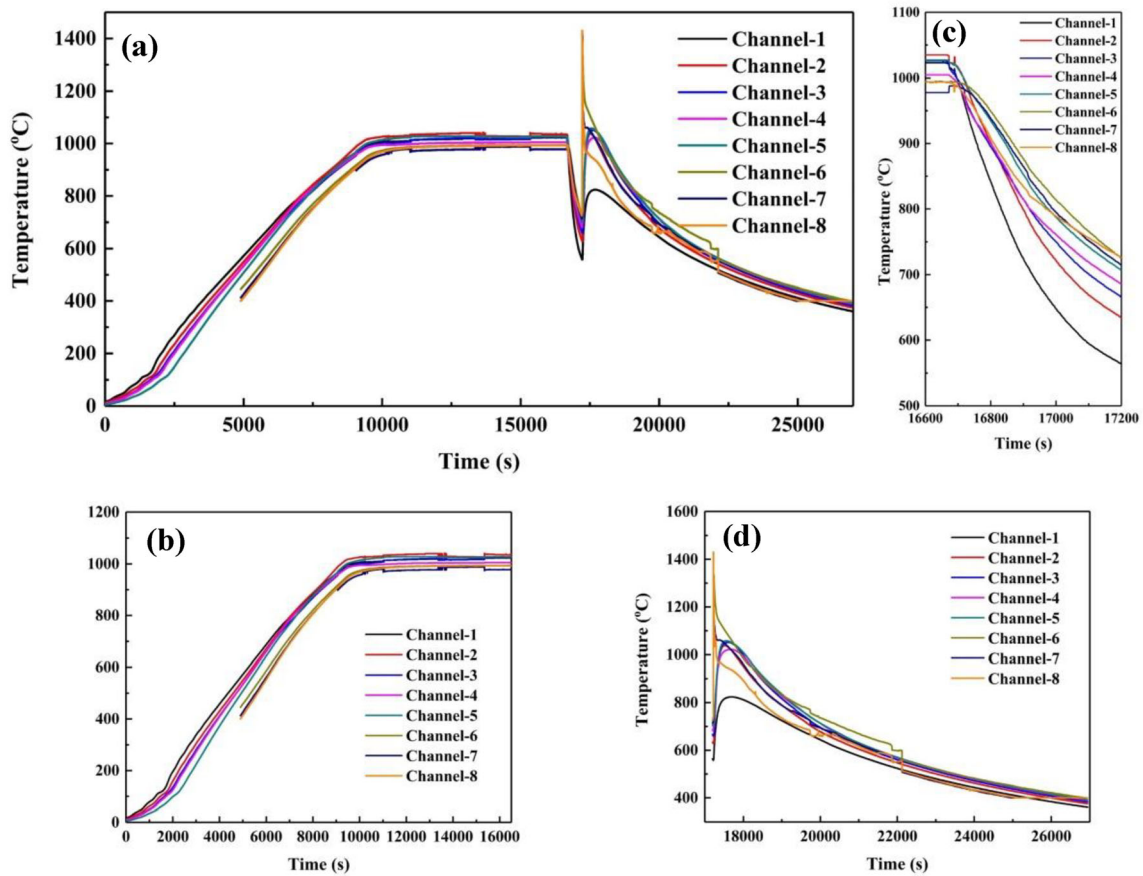


**Figure 5. Experimental temperature profiles of the thermocouples: (a) in all processes, (b) in the preheating and insulation process, (c) in the transferring process, (d) in the pouring and solidification process.**

And, the convergence is judged by:

$$|\Delta h_k / h_k| < \varepsilon \quad \text{Eqn. 11}$$

where the general value of  $\varepsilon$  is 0.001 or less.

## Results and Discussion

### Temperature Distribution During the Entire Process

The measured temperature in the casting and shell mold is shown in Figure 5(a). At the beginning of the temperature measurement, the shell mold was preheated to 1050 °C and held for approximately 7000 s to ensure temperature uniformity, as illustrated in Figure 5(b). The results show that during the preheating process, no significant difference was found in the temperature distribution at each location of the shell mold, while the temperature inside the cavity is always lower than that at the corresponding location of the shell mold. It is seen from Figure 5(b) that the temperature of the shell mold decreases faster than the temperature inside the cavity during the transfer of the shell mold to the casting chamber

of the vacuum furnace and vacuum extraction. The lowest temperature of the shell mold even reached 558 °C (point 1). The temperatures at the casting (points 5 to 8) in the cavity rise rapidly when the molten metal is poured into the mold, while the temperatures at the shell mold (points 1 to 4) rise slowly and are much lower than the temperature of the casting as shown in Figure 5(c). Furthermore, three stages of the alloy cooling curve can be observed in Figure 5(d), which is consistent with the results of Ahmadein<sup>22</sup> and.<sup>31</sup> Firstly, because the shell mold temperature is much lower than the melt temperature, the heat exchange between the melt and the shell mold is extremely intense and leads to a rapid decrease in the temperature of the melt above the liquidus. Then, the cooling rate slows down within the crystallization temperature interval due to the release of latent heat of crystallization. Finally, when the temperature was lower than the solidus, the temperature of the shell mold and casting gradually converged. After the temperature reaches 600 °C, with the formation of an air gap between the casting and the mold shell, the rate of temperature decrease of the casting gradually slows down as a result of the change in interface heat transfer pattern from thermal conduction to convection heat transfer.

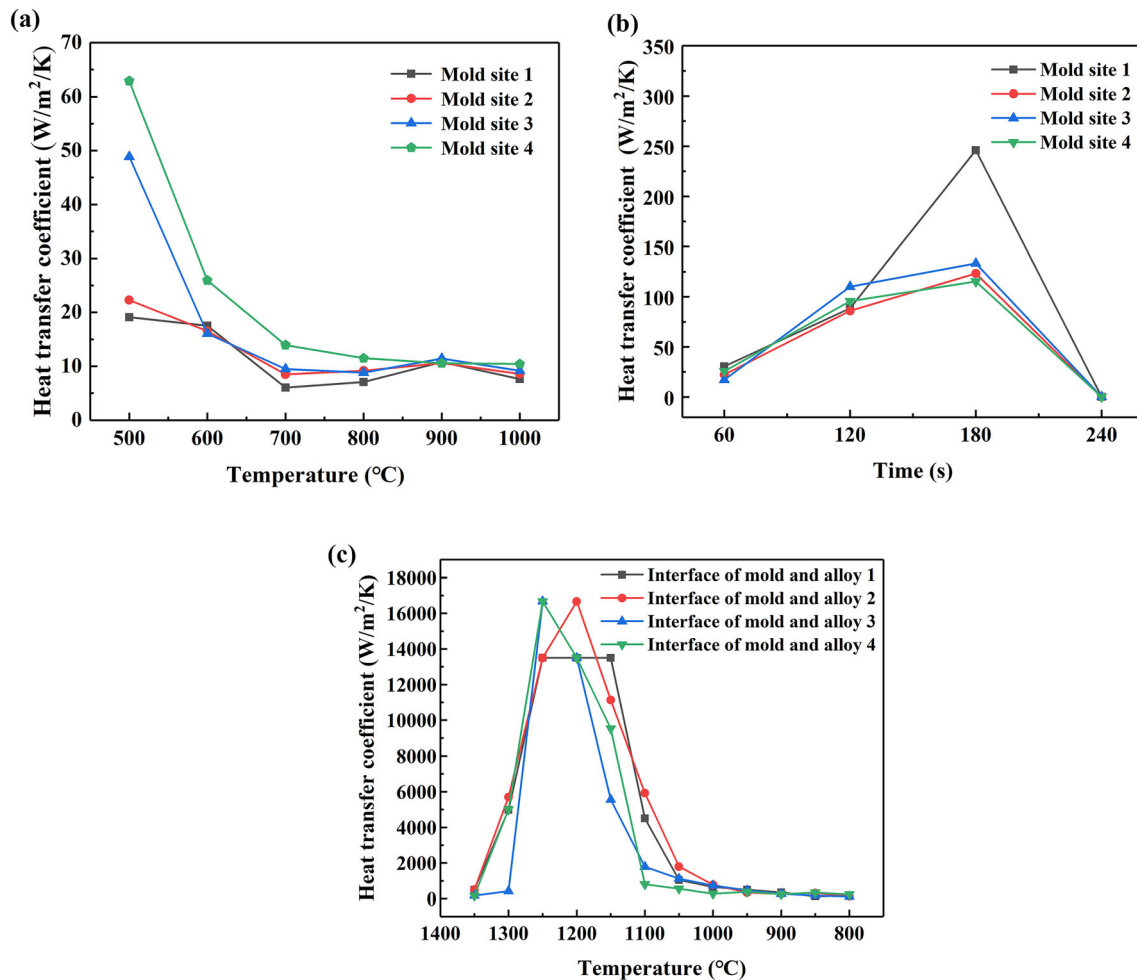


**Figure 6. Mold environment IHTC (a) during preheating process and (b) during transferring process, and (c) casting-mold IHTC during pouring and solidification process.**

### The Variation of IHTC Between Casting and Shell Mold

The inverse calculation results of casting-shell mold IHTC during the investment casting are plotted in Figure 6. During the preheating process, the initial IHTC between the shell mold and the furnace environment is high due to the strong convection of the air in the furnace during heat exchange near the colder shell mold, and the maximum IHTC can reach about 62 W/m<sup>2</sup>·K at point 4. Then, as the temperature of the shell mold increased, the heat exchange between the shell mold and furnace gradually weakened, so the IHTC decreased with decreasing temperature difference, as illustrated in Figure 6(a). In addition, the maximum temperature difference between the shell mold and the cavity during the preheating process is up to 100 °C, due to the fact that the interfacial heat transfer coefficient between the shell mold and the cavity remains constant close to 10 W/m<sup>2</sup>·K throughout the process. Finally, as the temperature approached the set temperature of 1050 °C, the temperature difference between the various locations decreases and the IHTC stabilized at to about 10 W/m<sup>2</sup>·K at all measurement locations. During the transfer of the shell mold to the casting

chamber and subsequent vacuum-pumping process, the IHTC continues to increase over the 120 seconds of transfer, due to the great temperature difference between the shell mold and the atmospheric environment, especially at the thinnest position of the shell mold where the IHTC even reaches 234.24 W/m<sup>2</sup>·K, which indicates that the interfacial heat transfer mode is transitioning from natural convection to forced convection during the transfer process. After 120 seconds, the IHTC first increases and then decreases with the rapid flow and loss of the heat transfer medium (air) during the vacuum-pumping process. When the vacuum level reaches 10<sup>-3</sup> Pa, the IHTC of the shell mold is stabilized at 0.1 W/m<sup>2</sup>·K, indicating that the interface heat transfer mode changes from convection to radiation.

Figure 6(c) presents the variation of IHTC during the pouring and solidification process. At the beginning of the pouring stage, the temperature difference between the melt and the shell mold is extremely large, according to Eqn. 1, the IHTC in this stage will not be too high, and the calculated results are close to the average value of IHTC between the ceramic shell and casting of 500 W/m<sup>2</sup>·K proposed by Kinrad<sup>32</sup> for IN 718 alloy.

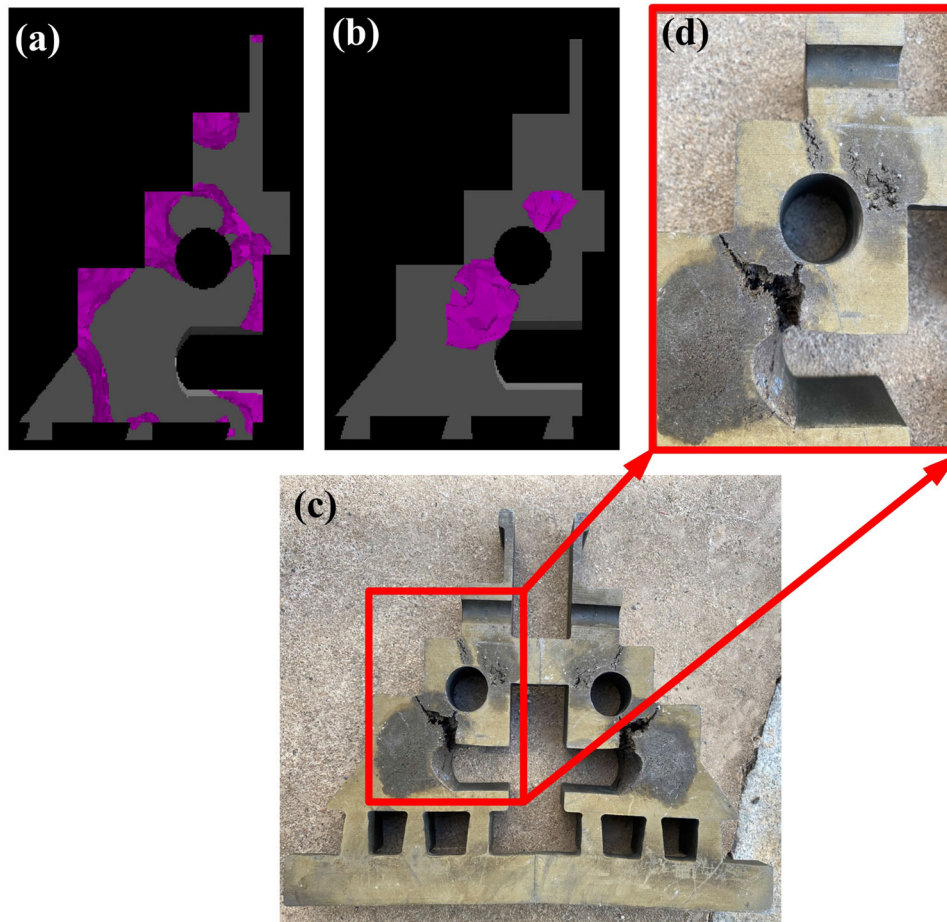


**Figure 7. (a) The defect position prediction obtained with  $IHTC = 500 \text{ W/m}^2\cdot\text{K}$ , (b) The defect position prediction obtained with  $IHTC q(t)$ , (c) and (d) the defects on casting in experiment.**

In the starting of solidification, the difference and complexity of grain orientation between fine grains led to the disorder of heat-flows direction, the IHTC kept at a lower value about 150 to  $500 \text{ W/m}^2\cdot\text{K}$ . During the subsequent solidification process, with the growth of columnar grain, the IHTC increases rapidly as a result of the single grain orientation of the columnar grain and the heat-flows direction and the decrease in the temperature difference between the melt and the shell mold. The maximum IHTC between the casting and the shell mold reached  $16000 \text{ W/m}^2\cdot\text{K}$ , which is close to the IHTC obtained by Zhang<sup>17</sup> during the solidification of A355 aluminum alloy investment casting. After solidification of the superalloy, i.e., at temperatures below  $1200 \text{ }^\circ\text{C}$ , the IHTC decreases with decreasing heat flow density and the formation of the gap, and stabilizes between 100 and  $200 \text{ W/m}^2\cdot\text{K}$  after temperatures below  $1100 \text{ }^\circ\text{C}$ . This is also in agreement with the findings of Sahai and Overfelt<sup>17,19</sup> in nickel-based alloy plate investment castings.

### Defect Prediction and Verification

To verify the accuracy of the inverse calculation results, IHTC values were applied in the ProCAST software for predicting the location and shape of shrinkage porosities, and the predicted results were compared with the experimental results. The IHTCs obtained by inverse calculations and the constant of  $500 \text{ W/m}^2\cdot\text{K}$  proposed by Kinrad<sup>32</sup> were substituted into ProCAST for defect prediction, respectively. The simulation results of shrinkage porosity obtained by different IHTCs are shown in Figure 7(a) and (b), and the experimental results are presented in Figure 7(c) and (d). Comparison results show that the shape and location of predicted shrinkage porosity using the IHTC proposed in this paper are basically consistent with the actual results, and it can be found the hot tears in the shrinkage range at right angles, but the calculated defect range is slightly smaller than the actual shrinkage range.



## Conclusions

The temperatures of the casting and ceramic shell in investment casting have been measured, and the IHTC during the investment casting of nickel-based superalloys has been investigated by inverse method and verified by means of experimental and simulation methods. The conclusions can be summarized as follows:

- (1) Due to the forced convection of air in the furnace near the colder shell mold, the maximum IHTC between the shell and the cavity at the beginning of heating can be up to about  $62 \text{ W/m}^2\cdot\text{K}$  during the heating process, and the IHTC decreased and the heat transfer approaches a steady state as the shell mold temperature increases. Finally, the IHTC remained at  $10 \text{ W/m}^2\cdot\text{K}$  when the shell mold temperature increased to  $1050^\circ\text{C}$ . In addition, the interfacial heat transfer coefficient between the shell mold and the cavity remained constant of  $10 \text{ W/m}^2\cdot\text{K}$  during the heating process.
- (2) The interfacial heat transfer between the shell mold and the atmospheric environment during the transfer process changes from natural convection to forced convection, and the IHTC increases to  $85$  to  $110 \text{ W/m}^2\cdot\text{K}$ . Then, the interface heat transfer mode between cavity and shell is changed from convection to radiation during the vacuum-pumping process after transferred to a vacuum casting chamber, the IHTC first increases and then decreases with the rapid flow and loss of the heat transfer medium (air), the maximum IHTC can be reached  $245.9 \text{ W/m}^2\cdot\text{K}$  at the thinnest position of the shell, and at last, the IHTC decreased to  $0.1 \text{ W/m}^2\cdot\text{K}$ .
- (3) The IHTC is about  $5000 \text{ W/m}^2\cdot\text{K}$  at the early stage of pouring process due to the large temperature difference between the melt and shell mold. With the release of latent heat of crystallization and the increase in temperature of shell mold, the heat flow density increases and the temperature difference between the melt and shell decreases, which leads to an increase in the IHTC up a maximum of  $16,000 \text{ W/m}^2\cdot\text{K}$ . Then, as the cooling proceeds, the IHTC gradually stabilizes at  $100$ – $200 \text{ W/m}^2\cdot\text{K}$ .
- (4) The prediction of shrinkage porosity defects adopting different IHTC were confirmed by the experiment. The verification result showed that the shrinkage defect locations can be effectively predicted by using the IHTC results obtained based on the inverse calculation, and its

simulation prediction results are in good agreement with the experimental results.

**Conflict of interest** The authors declare that they have no known competing financial interests or personal relationships that could have appeared to influence the work reported in this paper.

## REFERENCES

1. A. Gloria, R. Montanari, M. Richetta, A. Varone, Alloys for aeronautic applications: state of the art and perspectives. *Metals*. (2019). <https://doi.org/10.3390/met9060662>
2. S.K. Selvaraj, G. Sundaramali, S. Jithin Dev, R. Srii Swathish, R. Karthikeyan, K.E. Vijay Vishaal, V. Paramasivam, F. Kara, Recent advancements in the field of Ni-based superalloys. *Adv. Mater. Sci. Eng.* (2021). <https://doi.org/10.1155/2021/9723450>
3. T. Sonar, V. Balasubramanian, S. Malarvizhi, T. Venkateswaran, D. Sivakumar, An overview on welding of Inconel 718 alloy-Effect of welding processes on microstructural evolution and mechanical properties of joints. *Mater Charact* **174**, 22 (2021). <https://doi.org/10.1016/j.matchar.2021.110997>
4. J. Zhang, Z.Q. Jie, T.W. Huang, W.C. Yang, L. Liu, H.Z. Fu, Research and development of equiaxed grain solidification and forming technology for nickel-based cast superalloys. *Acta Metall. Sin.* **55**(9), 1145–1159 (2019)
5. Y.H. Zheng, Z.D. Wang, Development of casting process for thin walled complex-precision aluminum alloy castings. *Foundry*. **59**(8), 796–799 (2010). [https://doi.org/10.1016/S1875-5372\(10\)60130-0](https://doi.org/10.1016/S1875-5372(10)60130-0)
6. G.K. Upadhyaya, S. Das, U. Chandra, A.J. Paul, Modelling the investment casting process: A novel approach for view factor calculations and defect prediction. *Appl. Math. Modell.* **19**(6), 354–362 (1995). [https://doi.org/10.1016/0307-904X\(95\)90001-O](https://doi.org/10.1016/0307-904X(95)90001-O)
7. K. Cui, Q.Y. Xu, J. Yu, B.C. Liu, Radiative heat transfer calculation for superalloy turbine blade in directional solidification process. *Acta Metall. Sinica*. **43**(5), 465–471 (2007)
8. S. Kumar, D.B. Karunakar, Characterization and properties of ceramic shells in investment casting process. *Int. J. Metalcast.* **15**(1), 98–107 (2020). <https://doi.org/10.1007/s40962-020-00421-6>
9. Z. Xiao, Z. Lv, X. Zhou, J. Liu, Z. Ma, S. Nie, S. Dong, Numerical simulation and optimization of investment casting for complex thin-walled castings. *Int. J. Metalcast.* (2023). <https://doi.org/10.1007/s40962-023-00990-2>
10. X. Hao, G.H. Liu, Y. Wang, S.P. Wu, Z.D. Wang, Optimization of investment casting process for K477

- superalloy aero-engine turbine nozzle by simulation and experiment. *China Foundry*. **19**(4), 351–358 (2022). <https://doi.org/10.1007/s41230-022-1092-4>
11. S.S. Hu, Y.S. Zhao, W.M. Bai, X.M. Wang, F.C. Yin, W.C. Yang, L. Liu, Temperature field evolution of seeding during directional solidification of single-crystal Ni-based superalloy castings. *Metals*. **12**(5), 12 (2022). <https://doi.org/10.3390/met12050817>
  12. L. Qin, J. Shen, Q.D. Li, Z. Shang, Effects of convection patterns on freckle formation of directionally solidified Nickel-based superalloy casting with abruptly varying cross-sections. *J. Cryst. Growth* **466**, 45–55 (2017). <https://doi.org/10.1016/j.jcrysgro.2017.03.021>
  13. Q.Y. Sun, Y. Ren, D.R. Liu, Numerical investigations of freckles in directionally solidified nickel-based superalloy casting with abrupt contraction in cross section. *Results Phys*. **12**, 1547–1558 (2019). <https://doi.org/10.1016/j.rinp.2019.01.056>
  14. Y.P. Wei, B. Yu, Q.Z. Yang, P. Gao, J. Shi, Z.Q. Miao, J.C. Cheng, X. Sun, Numerical simulation and experimental validation on fabrication of nickel-based superalloy Kagome lattice sandwich structures. *China Foundry*. **17**(1), 21–28 (2020). <https://doi.org/10.1007/s41230-020-9100-z>
  15. Q.Y. Xu, B.C. Liu, Z.J. Liang, J.R. Li, S.Z. Liu, H.L. Yuan, Modeling of unidirectional growth in a single crystal turbine blade casting. *Mater. Sci. Forum* **508**, 111–116 (2006). <https://doi.org/10.4028/www.scientific.net/MSF.508.111>
  16. J. Yu, Q.Y. Xu, K. Cui, B.C. Liu, A. Kimatsuka, A. Kuroki, A. Hirata, Numerical simulation of solidification process on single crystal Ni-based superalloy investment castings. *J. Mater. Sci. Technol.* **23**(1), 47–54 (2007)
  17. W.H. Zhang, G.N. Xie, D. Zhang, Application of an optimization method and experiment in inverse determination of interfacial heat transfer coefficients in the blade casting process. *Exp. Thermal Fluid Sci.* **34**(8), 1068–1076 (2010). <https://doi.org/10.1016/j.expthermflusci.2010.03.009>
  18. M. Xu, S.N. Lekakh, V.L. Richards, Thermal property database for investment casting shells. *Int. J. Metalcast.* **10**(3), 329–337 (2016). <https://doi.org/10.1007/s40962-016-0052-4>
  19. W.D. Griffiths, K. Kawai, The effect of increased pressure on interfacial heat transfer in the aluminium gravity die casting process. *J. Mater. Sci.* **45**(9), 2330–2339 (2010). <https://doi.org/10.1007/s10853-009-4198-9>
  20. D. Szeliga, K. Kubiak, W. Ziaja, R. Cygan, J.S. Suchy, A. Burelko, W.J. Nowak, J. Sieniawski, Investigation of casting-ceramic shell mold interface thermal resistance during solidification process of nickel based superalloy. *Exp. Thermal Fluid Sci.* **87**, 149–160 (2017). <https://doi.org/10.1016/j.expthermflusci.2017.04.024>
  21. H. Shao, Y. Li, H. Nan, Y.Q. Xu, Research on the interfacial heat transfer coefficient between casting and ceramic shell in investment casting process of Ti6Al4V alloy ACTA metallurgica sinica. *Etallurgica Sinica*. **51**, 976–984 (2015)
  22. M. Ahmadein, B. Pustal, N. Wolff, A. Bührig-Polaczek, Determination and verification of the gap dependent heat transfer coefficient during permanent mold casting of A356 aluminum alloy. *Materialwiss. Werkstofftech.* **48**(12), 1249–1256 (2017). <https://doi.org/10.1002/mawe.201700153>
  23. P. Sharifi, J. Jamali, K. Sadayappan, J.T. Wood, Grain size distribution and interfacial heat transfer coefficient during solidification of magnesium alloys using high pressure die casting process. *J. Mater. Sci. Technol.* **34**(2), 324–334 (2018). <https://doi.org/10.1016/j.jmst.2016.09.004>
  24. P. Tao, H. Shao, Z. Ji, H. Nan, Q. Xu, Numerical simulation for the investment casting process of a large-size titanium alloy thin-wall casing. *Progress Natl. Sci. Mater. Int.* **28**(4), 520–528 (2018). <https://doi.org/10.1016/j.pnsc.2018.06.005>
  25. Z. Guo, J.X. Zhou, Y.J. Yin, X. Sheng, X.Y. Ji, Numerical simulation of directional solidification of superalloys based on modified difference mesh. *Special Cast. Nonferrous Alloys*. **55**(5), 613–618 (2019)
  26. M. Lamm, R.F. Singer, The effect of casting conditions on the high-cycle fatigue properties of the single-crystal nickel-base superalloy PWA 1483. *Metall. Mater. Trans. Phys. Metall. Mater. Sci.* **38A**(6), 1177–1183 (2007). <https://doi.org/10.1007/s11661-007-9188-4>
  27. Y. Wang, S.P. Wu, X. Xue, R.R. Chen, J.B. Zhang, W.F. Xiao, Formation mechanism and criterion of linear segregation in ZL205A alloy. *Trans. Nonferrous Metals Soc. China*. **24**(11), 3632–3638 (2014). [https://doi.org/10.1016/s1003-6326\(14\)63508-1](https://doi.org/10.1016/s1003-6326(14)63508-1)
  28. G. Milano, F. Scarpa, Università di Genova, Italia, Private Communication, 1994.
  29. M. Cross, J. Campbell. Modeling of casting, welding and advanced solidification processes, (1995).
  30. J.M. Drezet, M. Rappaz, G.-U.G. Gremaud, Determination of thermophysical properties and boundary conditions of direct chill-cast aluminum alloys using inverse methods. *Metall. Mater. Trans. A* **31**(6), 1627–1634 (2000). <https://doi.org/10.1007/s11661-000-0172-5>
  31. A. Hamasaid, M.S. Dargusch, G. Dour, The impact of the casting thickness on the interfacial heat transfer and solidification of the casting during permanent mold casting of an A356 alloy. *J. Manuf. Process.* **47**,

229–237 (2019). <https://doi.org/10.1016/j.jmapro.2019.09.039>

32. C.H. Konrad, M. Brunner, K. Kyrgyzbaev, R. Volkl, U. Glatzel, Determination of heat transfer coefficient and ceramic mold material parameters for alloy IN738LC investment castings. *J. Mater. Process. Technol.* **211**(2), 181–186 (2011). <https://doi.org/10.1016/j.jmatprotec.2010.08.031>

**Publisher's Note** Springer Nature remains neutral with regard to jurisdictional claims in published maps and institutional affiliations.

Springer Nature or its licensor (e.g. a society or other partner) holds exclusive rights to this article under a publishing agreement with the author(s) or other rightsholder(s); author self-archiving of the accepted manuscript version of this article is solely governed by the terms of such publishing agreement and applicable law.